# Electron-paramagnetic-resonance investigation of the dynamic Jahn-Teller effect for $Sc^{2+}$ in $BaF_2$, $SrF_2$, and $CaF_2$

J. R. Herrington*†
*Institut für Angewandte Festkörperphysik der Fraunhofer-Gesellschaft, 78 Freiburg im Breisgau, Bundesrepublik Deutschland, West Germany*

L. A. Boatner
*Advanced Technology Center, Incorporated, Dallas, Texas 75222*

T. J. Aton*‡ and T. L. Estle*
*Physics Department, Rice University, Houston, Texas 77001*
(Received 25 February 1974)

The EPR spectrum of $Sc^{2+}$ has been observed in single crystals of $BaF_2$, $SrF_2$, and $CaF_2$ at liquid-helium temperatures. At 1.2 K, the spectra were characterized by intense anisotropic hyperfine patterns with partially resolved ligand hyperfine structure. The anisotropy, line shapes, and temperature dependence of the anisotropic spectrum obtained for each host crystal were described within experimental error by second-order solutions of an effective Hamiltonian for an isolated vibronic $^2E$ state which is split by large random internal strains. Coexisting with the anisotropic pattern was a weak nearly isotropic hyperfine pattern with "conventional" line shapes. No ligand hyperfine structure was resolved on this pattern. Intensity variations as a function of temperature imply that the nearly isotropic structure results from averaging by rapid vibronic relaxation of a portion of the anisotropic pattern. This interpretation is further strengthened by the observation of a small predicted anisotropy. Observed deviations of effective Hamiltonian parameters from the values predicted by crystal-field theory imply the existence of a weak-to-moderate vibronic interaction for these systems, i.e., a dynamic Jahn-Teller effect. For $d^1$-configuration ions in cubic symmetry, the effective Hamiltonian parameters are summarized and discussed.

## I. INTRODUCTION

The Jahn-Teller theorem[1] states that a symmetric nonlinear polyatomic complex in an orbitally degenerate electronic state is unstable with respect to at least one asymmetric distortion which removes the orbital degeneracy. For ions in solids, the fundamental mechanism for the Jahn-Teller effect is the Coulomb interaction which couples the orbitally degenerate electronic states of the complex to lattice vibrations.[2,3]

The early low-temperature electron-paramagnetic-resonance (EPR) data for ions with orbital-doublet ground states were, in general, consistent with the concept of a static Jahn-Teller effect.[2,3] Later, however, results were obtained at low temperatures for $Cu^{2+}$ in MgO[4-6] and CaO[7] and for $Sc^{2+}$ in $CaF_2$ and $SrF_2$[8,9] which were not characteristic of the static Jahn-Teller effect. These data were initially interpreted using a strong vibronic coupling model[10-12] with tunneling through potential barriers separating the "static" Jahn-Teller configurations. Subsequently, Ham[3,13] proposed a new interpretation of the EPR spectra observed for the $CaF_2:Sc^{2+}$ and $SrF_2:Sc^{2+}$ systems. He demonstrated that these data did not necessarily imply the large Jahn-Teller stabilization energies previously assumed, and that, in fact, the experimental parameters describing the $Sc^{2+}$ EPR data implied weak vibronic coupling.

Somewhat later Chase,[14,15] in his study of the EPR spectrum observed from an excited orbital doublet of $Eu^{2+}$ in $CaF_2$, found that when the vibronic coupling and random strain were sufficiently strong, interaction with an excited vibronic singlet could selectively broaden certain features of the EPR spectrum. Chase suggested[14] that this selective broadening might play a role in the $CaF_2:Sc^{2+}$ spectrum.

In our EPR investigations[16-19] of $La^{2+}$, $Y^{2+}$, and $Sc^{2+}$ in $SrCl_2$, we found that the spectra observed for these systems were adequately described by an isolated vibronic doublet formalism which implied weak-to-moderate vibronic coupling.[3,13] In view of the uncertainty in previous interpretations[3,8,9,13,14] of the $Sc^{2+}$ EPR data, the new theoretical insights provided by Ham[3,13] and Chase,[14,15] and the experience gained from our earlier EPR experiments,[16-19] a decision was made to reinvestigate $Sc^{2+}$ in $CaF_2$ and $SrF_2$ and, in addition, to investigate $Sc^{2+}$ in $BaF_2$. These data permit an extension of our systematic study[16-19] of the dynamic Jahn-Teller effect for divalent ions with $d^1$ configurations in eightfold coordination and extend the results given in a preliminary report.[20]

## II. THEORY

The weak-to-moderate vibronic coupling model and the associated effective Hamiltonian formalism

developed by Ham[3,13] describe the line shapes, angular dependence, and temperature dependence of the EPR spectrum for an isolated vibronic doublet. Ham[3,13] has also given expressions for estimating the Jahn-Teller stabilization energy and hence the strength of the vibronic interaction and has demonstrated the importance of random internal strains.

For completeness, the effective Hamiltonian for an isolated $^2E$ state will be reviewed here, but the reader is referred to earlier papers[3,13,16-19] for a more extensive treatment.

An effective Hamiltonian representing the random strain, Zeeman, hyperfine and quadrupole[18] interactions for a $^2E$ state in cubic symmetry is given in Eq. (1):

$$\begin{aligned} H = {} & qV_s(e_\theta \mathcal{E}_\theta + e_\epsilon \mathcal{E}_\epsilon) + g_1\mu_B \vec{H}\cdot\vec{S}\mathfrak{a}_1 + A_1\vec{I}\cdot\vec{S}\mathfrak{a}_1 \\ & + \tfrac{1}{2}qg_2\mu_B[(3H_zS_z - \vec{H}\cdot\vec{S})\mathcal{E}_\theta + \sqrt{3}\,(H_xS_x - H_yS_y)\mathcal{E}_\epsilon] \\ & + \tfrac{1}{2}qA_2[(3I_zS_z - \vec{I}\cdot\vec{S})\mathcal{E}_\theta + \sqrt{3}\,(I_xS_x - I_yS_y)\mathcal{E}_\epsilon] \\ & + \tfrac{1}{2}qQ[(3I_zI_z - \vec{I}\cdot\vec{I})\mathcal{E}_\theta + \sqrt{3}\,(I_xI_x - I_yI_y)\mathcal{E}_\epsilon] . \end{aligned} \quad (1)$$

Here, $\mathfrak{a}_1$, $\mathcal{E}_\theta$, and $\mathcal{E}_\epsilon$ are vibronic operators,[3-13] $e_\theta = \frac{1}{2}(2e_{zz} - e_{xx} - e_{yy})$, and $e_\epsilon = \frac{1}{2}\sqrt{3}\,(e_{xx} - e_{yy})$ are symmetrized strain components, $\vec{H}$ is the magnetic field, $\vec{S}$ is the electronic spin operator, and $\vec{I}$ is the nuclear spin operator. The parameters, $qV_s$, $g_1\mu_B$, $A_1$, $\frac{1}{2}qg_2\mu_B$, $\frac{1}{2}qA_2$ and $\frac{1}{2}qQ$ represent the relative strengths of the various terms, and the reduction factor[3,13] $q$ is included explicitly in the appropriate parameters.

When the strain interaction determines the composition of the vibronic states,[3,13,17-19] the EPR transitions occur within the two resultant Kramers doublets. These EPR transition frequencies are given to second order[19] in Eq. (2):

$$\begin{aligned} h\nu_\pm = {} & \left(g_1 \pm \tfrac{1}{2}qg_2f_1 + \frac{(qg_2)^2}{g_1}f_3\right)\mu_BH \\ & + \left(A_1 \pm \tfrac{1}{2}qA_2f_1 + \frac{(qA_2)^2}{A_1}f_3 + 2\frac{qg_2}{g_1}qA_2f_3 \right. \\ & \left. + \frac{4(qQ)^2}{A_1}[(f_3 - f_4) + 2(f_4 - 2f_3)I(I+1)]\right)M_I \\ & + \left(\frac{(A_1 \mp \frac{1}{4}qA_2f_1)^2}{2g_1\mu_BH} + \frac{(qA_2)^2}{g_1\mu_BH}f_4\right)[I(I+1) - M_I^2] \\ & + \frac{(qA_2)^2}{g_1\mu_BH}f_3M_I^2 + \frac{8(qQ)^2}{A_1}(2f_3 - f_4)M_I^3 , \end{aligned} \quad (2)$$

where the two signs differentiate between the strain-produced Kramers doublets. The functions $f_1$, $f_3$, and $f_4$ are given in Eqs. (3)–(5):

$$f_1 = (3n^2 - 1)\cos\phi + \sqrt{3}\,(l^2 - m^2)\sin\phi , \quad (3)$$

$$\begin{aligned} f_3 = {} & \tfrac{1}{8}\{2 - [(3n^2 - 1)\cos\phi + \sqrt{3}\,(l^2 - m^2)\sin\phi]^2 \\ & - [-(3n^2 - 1)\cos2\phi + \sqrt{3}\,(l^2 - m^2)\sin2\phi]\} , \end{aligned} \quad (4)$$

$$\begin{aligned} f_4 = {} & \tfrac{1}{32}\{4 + [(3n^2 - 1)\cos\phi + \sqrt{3}\,(l^2 - m^2)\sin\phi]^2 \\ & + 4[-(3n^2 - 1)\cos2\phi + \sqrt{3}\,(l^2 - m^2)\sin2\phi]\} . \end{aligned} \quad (5)$$

Here, $l$, $m$, and $n$ are the direction cosines of the magnetic field with respect to the ⟨100⟩ axes, and $\tan\phi = e_\epsilon/e_\theta$.

When the composition of the vibronic states is determined by the anisotropic parts of the Zeeman and hyperfine interactions and not the strain interaction, then the frequencies for the two most-intense transitions are also given by Eq. (2), but with the following definitions of $f_1$, $f_3$, and $f_4$ which apply only in {110} planes:

$$f_1 = 1 - 3n^2 , \quad (6)$$

$$f_3 = \tfrac{3}{8}(1 - n^2)(3n^2 + 1) , \quad (7)$$

$$f_4 = \tfrac{3}{8}n^2 + \tfrac{9}{32}(1 - n^2)^2 . \quad (8)$$

As before, $n$ is the cosine of the angle between the magnetic field and the ⟨100⟩ axis in the particular {110} plane. The two signs in Eq. (2) now refer to transitions within the Kramers doublets produced by the anisotropic terms in the effective Hamiltonian.

The inclusion of a weak isotropic ligand hyperfine interaction in the effective Hamiltonian results in a splitting of each hyperfine transition into a symmetric series of transitions. This situation is illustrated in Fig. 1 for the $M_I = -\frac{5}{2}$ hyperfine components. Assuming that all values of the strain angle $\phi$ occur with equal probability, neglecting all second-order terms, and not including ligand hyperfine structure, the microwave absorption predicted by Eq. (2) is shown in Figs. 1(a) and 1(b). The effect of a weak isotropic hyperfine interaction with eight ligand nuclei of spin $\frac{1}{2}$ is shown schematically in Figs. 1(c) and 1(d). Each of the hyperfine components such as those in Figs. 1(a) and 1(b) is split into nine lines whose relative intensities are given by the ratios 1 : 8 : 28 : 56 : 70 : 56 : 28 : 8 : 1. This results in nine overlapping envelopes with the above relative intensities. A first derivative of the envelopes of Figs. 1(c) and 1(d) will have partially resolved ligand hyperfine structure near each of the two extremes of the envelopes. However, it is evident that the ligand hyperfine structure patterns depend on the exact shape of the original hyperfine envelopes.

In second order, the line shape of the individual hyperfine components becomes asymmetric.[17,19] For $\vec{H} \parallel \langle 100\rangle$, this asymmetry is produced by those terms in Eq. (2) which are multiplied by $f_4$ and by the $(qg_2f_1/g_1)^2$ term in the expansion of $1/(g_1 \pm \frac{1}{2}qg_2f_1)$, although these terms are small. For magnetic field orientations away from $\vec{H} \parallel \langle 100\rangle$, the $(qA_2)^2f_3/A_1$ term[19] will produce an effect larger

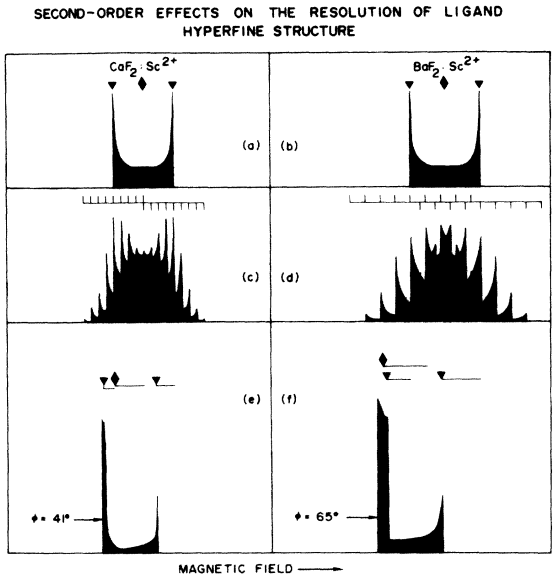


FIG. 1. Shown in this schematic representation of the most extreme effects of second-order terms in Eq. (2) on the appearance of ligand hyperfine structure are: the line shapes predicted in first-order for the $M_I = -\frac{5}{2}$ hyperfine component of the EPR spectrum, $\vec{H} \parallel \langle 110 \rangle$, for (a) $CaF_2:Sc^{2+}$ and (b) $BaF_2:Sc^{2+}$; the line shape predicted in first order including an isotropic ligand hyperfine interaction for the $M_I = -\frac{5}{2}$ hyperfine component, $\vec{H} \parallel \langle 110 \rangle$, for (c) $CaF_2:Sc^{2+}$ and (d) $BaF_2:Sc^{2+}$; and the line shape predicted in second-order for the $M_I = -\frac{5}{2}$ hyperfine component, $\vec{H} \parallel \langle 110 \rangle$, for (e) $CaF_2:Sc^{2+}$ and (f) $BaF_2:Sc^{2+}$. The microwave absorption is plotted versus magnetic field with the individual transitions represented as $\delta$ functions. The solid diamonds represent the field positions for $\phi = \pm\frac{1}{2}\pi, \pm\frac{3}{2}\pi$. The solid triangles represent the field positions for $\phi = 0, \pm\pi$. Horizontal scales in (c) and (d) represent locations of the ligand hyperfine pattern at the two extremes of the absorption. The displacements of the diamond and triangle symbols in (e) and (f) indicated by horizontal lines show the difference between the prediction in first-order and those in second-order. The values of the strain angular parameter $\phi$ locating the low-field extremes of the absorption in (e) and (f) are shown.

than the other second-order terms. For $Sc^{2+}$ in $SrCl_2$,[19] this $(qA_2)^2 f_3/A_1$ term produced large effects on the line shapes.

To illustrate the most extreme influence of second-order effects on the ligand hyperfine structure, the line shapes (without ligand hyperfine structure) of the $M_I = -\frac{5}{2}$ hyperfine components are shown in Figs. 1(e) and 1(f). Nine overlapping envelopes of the type shown in Figs. 1(e) and 1(f) would greatly complicate the ligand hyperfine spectrum because of the three-peaked character of the absorption. The solid triangles locate the positions of the EPR transitions for $\phi = 0, \pm\pi$, and the solid diamonds locate the EPR transitions for $\phi = \frac{1}{2}\pi, \pm\frac{3}{2}\pi$. The shifts produced by second-order terms for $\phi = 0, \pm\pi$ and $\phi = \pm\frac{1}{2}\pi$ are represented by the horizontal displacements shown in Figs. 1(e) and 1(f). The value of $\phi$ for the low-field extreme is also given. Second-order effects are much less drastic for other orientations and other hyperfine components.

Rapid vibronic relaxation (i.e., $\Delta M_S = 0$) between the two strain-produced Kramers doublets can result in microwave absorption midway between the positions of the two EPR transitions from the two doublets.[3,13] The intensities of these "average" transitions depend, in general, on the orientation of the applied magnetic field.[16–19] For a given magnetic field orientation, variations in intensities with $M_I$ are also observed.[16] In addition, it has been shown that certain second-order terms in Eq. (2) can produce small characteristic anisotropies for these transitions.

For ligand hyperfine structure to be resolved on the averaged lines the following conditions must hold: (i) the linewidth of the individual EPR transitions composing the envelopes must be smaller than the spacing between adjacent ligand hyperfine lines (at high temperatures this linewidth may result from spin-lattice relaxation), and (ii) the vibronic relaxation rate must be much greater than $2\pi\Delta\nu$ where $\Delta\nu$ is the maximum difference in frequency for the transitions resulting from the two strain-produced doublets.

## III. EXPERIMENTAL RESULTS AND DISCUSSION

Commercially available $CaF_2$, $SrF_2$, and $BaF_2$ single crystals were doped with Sc using the diffusion technique described by Höchli.[9] The divalent charge state of Sc was produced by either x or $\gamma$ irradiation at room temperature. EPR spectra were recorded using a back-reflection ($X$ band, 9 GHz) spectrometer with backward-diode detection. The microwave frequency was measured electronically, and magnetic field measurements were made with an NMR gaussmeter. Precision orientation of the magnetic field relative to the crystallographic axes was achieved using independent orthogonal rotations of the sample and magnet.

### A. Low-temperature anisotropic spectra

The EPR spectra observed at 1.2 K from irradiated $CaF_2:Sc$, $SrF_2:Sc$, and $BaF_2:Sc$ single crystals are shown in Figs. 2–4, respectively, for the applied magnetic field parallel to the three principal crystallographic directions, i.e., $\langle 100 \rangle$, $\langle 111 \rangle$, and $\langle 110 \rangle$. For a general direction of the applied magnetic field, each EPR spectrum consisted of eight anisotropic hyperfine components whose line shapes resulted from large random internal strains. The extremes of these line shapes

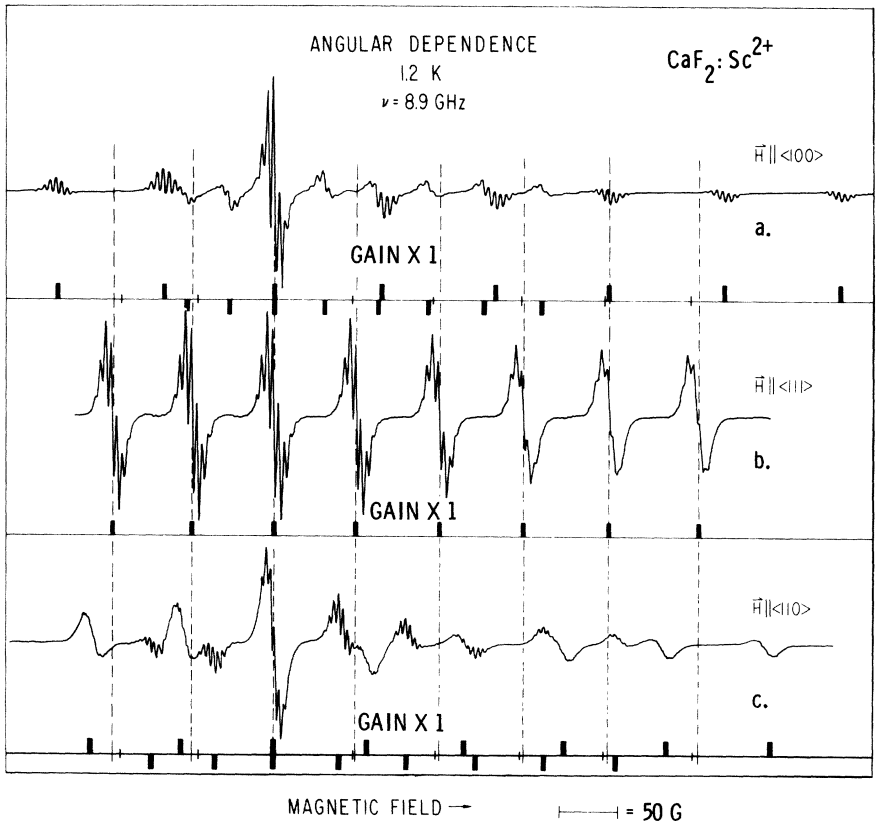


FIG. 2. EPR spectrum observed ($\nu = 8.9$ GHz) at 1.2 K for a reduced $CaF_2:Sc^{2+}$ sample. The first-derivative presentation of absorption is shown versus magnetic field for: (a) $\vec{H} \parallel \langle 100 \rangle$, (b) $\vec{H} \parallel \langle 111 \rangle$, and (c) $\vec{H} \parallel \langle 110 \rangle$. The extremes of the anisotropic hyperfine components are designated by broad vertical bars. The dashed vertical lines locate the positions of the eight hyperfine lines observed for $\vec{H} \parallel \langle 111 \rangle$. The positions of the eight features produced by averaging by rapid vibronic relaxation are indicated in (a) and (c) by small vertical lines.

were described, in first order, by the cubic anisotropy function $[1-3(l^2m^2+m^2n^2+n^2l^2)]^{1/2}$. The importance of second-order terms is indicated by the observation that the line positions for $\vec{H} \parallel \langle 111 \rangle$ (indicated by dashed vertical lines in Figs. 2–4) differ from the average of the two extremes for the corresponding hyperfine components for $\vec{H} \parallel \langle 100 \rangle$ or $\vec{H} \parallel \langle 110 \rangle$. In Fig. 2, the average field positions of the extremes of the eight hyperfine components for $\vec{H} \parallel \langle 100 \rangle$ and $\vec{H} \parallel \langle 110 \rangle$ are indicated by narrow vertical bars on the horizontal scales below the traces. The extremes of the components in Figs. 2–4 are indicated by broad vertical bars on the horizontal scales below the traces.

Ligand hyperfine structure was partially resolved near the extremes of each hyperfine component although it is better resolved on one of the extremes. For $\vec{H} \parallel \langle 111 \rangle$ [see Figs. 2(b), 3(b), and 4(b)] as many as nine separate ligand hyperfine lines were resolved with relative intensities which are given approximately by the 1 : 8 : 28 : 56 : 70 : 56 : 28 : 8 : 1 ratios expected for a ligand hyperfine interaction with eight equivalent nuclei of spin $\frac{1}{2}$. In the fluorite structure, the $^{19}F$ ligands for a substitutional ion are not all magnetically equivalent for $\vec{H} \parallel \langle 111 \rangle$, but the data suggest that the anisotropy in the ligand hyperfine interaction may be neglected for the purposes of this work. As the direction of the magnetic field was varied, the ligand hyperfine splittings were observed to be approximately constant, but the relative intensities of the ligand hyperfine lines did vary. The observed ligand hyperfine splittings ($A_{LHFS}$) for the three systems are listed in Table I. The decrease in $A_{LHFS}$ in the order $CaF_2:Sc^{2+}$, $SrF_2:Sc^{2+}$, and $BaF_2:Sc^{2+}$ is expected since the host lattice constant (and hence the nearest-neighbor distance for these hosts) increases in that order.

The angular dependence of the central line of the ligand hyperfine structure at each extreme (or an estimate of its position when ligand hyperfine structure was not resolved) is shown in Figs. 5–7 for $CaF_2:Sc^{2+}$, $SrF_2:Sc^{2+}$, and $BaF_2:Sc^{2+}$, respectively. The measured field positions are represented by open circles. The solid curves in each figure are computed using the second-order solution of the effective Hamiltonian for an isolated $^2E$ state in the large random strain approximation, i.e., Eq. (2), and the appropriate parameters listed in Table I. The error limits listed in Table I were chosen to reflect the precision with which the extremes having no resolved ligand hyperfine structure could be measured.

From Figs. 2(b), 3(b), and 4(b), it is apparent that the linewidths of different hyperfine lines for

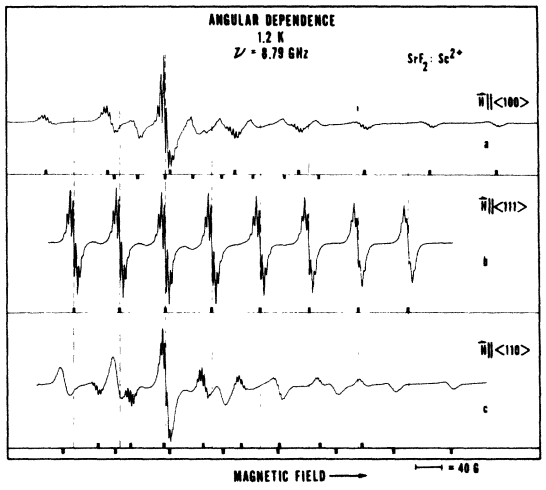


FIG. 3. EPR spectrum observed ($\nu = 8.8$ GHz) at 1.2 K for a reduced $SrF_2:Sc^{2+}$ sample. The first-derivative presentation of absorption is shown versus magnetic field for: (a) $\vec{H} \parallel \langle 100 \rangle$, (b) $\vec{H} \parallel \langle 111 \rangle$, and (c) $\vec{H} \parallel \langle 110 \rangle$. The vertical bars locate the extremes of the anisotropic hyperfine components. The dashed vertical lines locate the eight hyperfine lines observed for $\vec{H} \parallel \langle 111 \rangle$.

the same system are unequal for $\vec{H} \parallel \langle 111 \rangle$. Although this could result from mosaic structure,[17] it may be the result of a variation in the magnitude of the ratio, $qV_s(e_\delta^2+e_\epsilon^2)^{1/2}/(qg_2\mu_B H+qA_2M_I)$. If all complexes do not satisfy the large random strain condition, then second order terms will result in a distribution of line positions. This intensity variation has been observed in $SrCl_2:La^{2+}$, $SrCl_2:Y^{2+}$, $SrCl_2:Sc^{2+}$, $CaF_2:Sc^{2+}$, $SrF_2:Sc^{2+}$, and $BaF_2:Sc^{2+}$.

For $\vec{H} \parallel \langle 111 \rangle$, seven additional weak features were observed at 1.2 K. These additional lines occurred approximately halfway between adjacent hyperfine lines. Their positions and intensities are characteristic of $\Delta M_S = \pm 1$, $\Delta M_I = \pm 1$ transitions and, as previously reported,[18] imply the existence of a weak nuclear electric quadrupole interaction for the isolated $^2E$ state in cubic symmetry.

### B. Temperature dependence between 1.2 and 4.2 K

The temperature dependences of the EPR spectra observed for $CaF_2:Sc^{2+}$, $SrF_2:Sc^{2+}$, and $BaF_2:Sc^{2+}$ are shown in Figs. 8–10, respectively. As seen in these figures, a weak eight-line pattern was observed to coexist with the anisotropic pattern discussed above. These lines are located in Figs. 8–10 by dashed vertical lines, and they were observed to increase in apparent intensity (the peak-to-peak amplitude in a first-derivative presentation) as the applied magnetic field was rotated in a $\{110\}$ plane toward a $\langle 111 \rangle$ axis. The intensity of each individual line depended on its relative position in the eight-line pattern. As the temperature was increased from 1.2 to 4.2 K, the intensities of each of these lines increased approximately linearly with temperature, and this increase was accompanied by the gradual broadening of the ligand

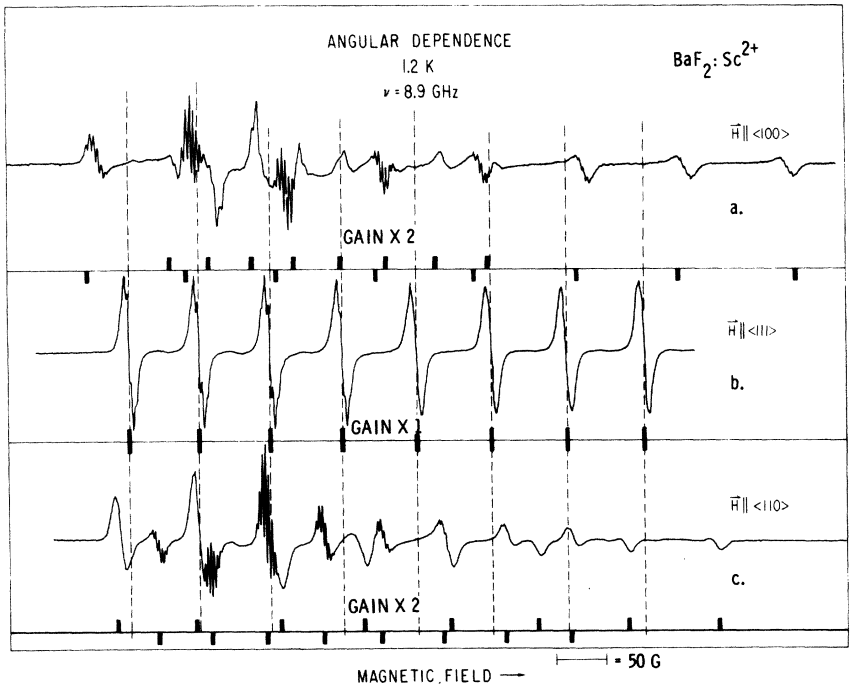


FIG. 4. EPR spectrum observed ($\nu = 8.9$ GHz) at 1.2 K for a reduced $BaF_2:Sc^{2+}$ sample. The first-derivative presentation of absorption is shown versus magnetic field for: (a) $\vec{H} \parallel \langle 100 \rangle$, (b) $\vec{H} \parallel \langle 111 \rangle$, and (c) $\vec{H} \parallel \langle 110 \rangle$. The vertical bars locate the extremes of the anisotropic hyperfine components. The dashed vertical lines locate the eight hyperfine lines observed for $\vec{H} \parallel \langle 111 \rangle$.

TABLE I. Effective Hamiltonian parameters for $d^1$-configuration ions exhibiting a dynamic Jahn-Teller effect in alkaline-earth halides. All experimental error limits are expressed in parentheses and should be added or subtracted from the last digit of the parameter.

| Host : Ion | $g_1$ | $qg_2$ | $A_1$ ($10^{-4}$ cm$^{-1}$) | $qA_2$ ($10^{-4}$ cm$^{-1}$) | $qQ$ ($10^{-4}$ cm$^{-1}$) | $A_{LHFS}$ (G) |
|---|---|---|---|---|---|---|
| $BaF_2:{}^{45}Sc^{2+}$ | 1.9555(8)[a] | −0.0309(8)[a] | −68.3(8)[a] | −24.5(8)[a] | −0.12(8)[b,a] | 3.8(5)[a] |
| $SrF_2:{}^{45}Sc^{2+}$ | 1.9640(5)[a] | −0.0240(5)[a] | −67.5(5)[a] | −24.3(5)[a] | −0.12(5)[b,a] | 4.7(3)[a] |
| $CaF_2:{}^{45}Sc^{2+}$ | 1.9719(5)[a] | −0.0211(5)[a] | −65.8(5)[a] | −24.1(5)[a] | −0.12(5)[b,a] | 5.0(3)[a] |
| $SrCl_2:{}^{45}Sc^{2+}$ | 1.953(1)[c] | −0.0442(8)[c] | −62.7(8)[c] | −31.5(5)[c] | −0.20(5)[b,c] | ... |
| $SrCl_2:{}^{89}Y^{2+}$ | 1.929(1)[c] | −0.0478(8)[c] | +24.3(8)[c] | +5.0(8)[c] | ... | ... |
| $SrCl_2:{}^{138}La^{2+}$ | ... | ... | −110(2)[b,d] | ... | ... | ... |
| $SrCl_2:{}^{139}La^{2+}$ | 1.881(1)[d] | −0.0687(8)[d] | −119.5(8)[d] | −18.8(8)[d] | +0.15(5)[b,d] | ... |

[a]This paper. [b]Reference 18. [c]Reference 19. [d]Reference 17.

hyperfine structure near the extremes of the anisotropic pattern. At temperatures near 77 K, the weak pattern dominates the EPR spectrum, and the anisotropic pattern has broadened beyond detection. These characteristics imply that the origin of these patterns is averaging by rapid vibronic relaxation. This interpretation was also consistent with the observation[18] that the positions of these lines for $\vec{H} \parallel \langle 100 \rangle$ differed from the positions for $\vec{H} \parallel \langle 111 \rangle$. These deviations, which occurred primarily in the hyperfine splittings, are illustrated in Fig. 9 for $SrF_2:Sc^{2+}$ where the components of the weak pattern are located by dashed vertical lines, and solid vertical lines locate the hyperfine lines observed for $\vec{H} \parallel \langle 111 \rangle$. These deviations are a result of the $(qA_2)^2 f_3/A_1$ term in Eq. (2), which

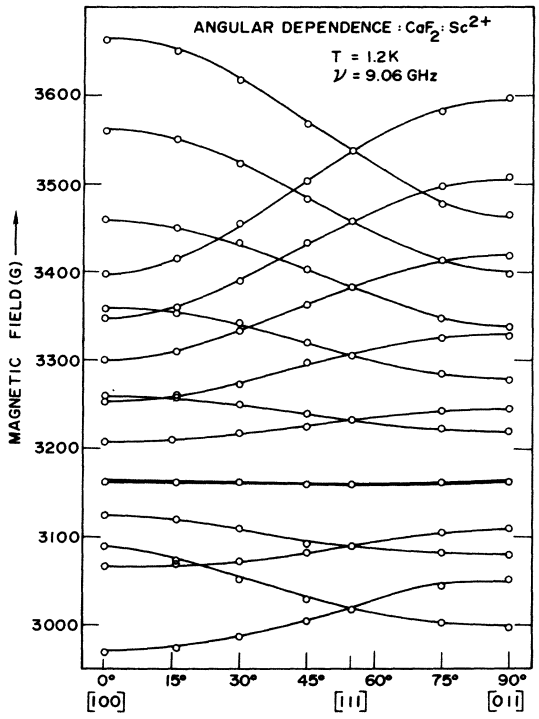


FIG. 5. Angular dependence of the extremes for the anisotropic pattern observed for $CaF_2:Sc^{2+}$. The open circles are experimental measurements and the solid curves were computed using the parameters in Table I for $CaF_2:Sc^{2+}$ and Eq. (2). All values of the strain angular variable $\phi$ were assumed to occur with equal probability.

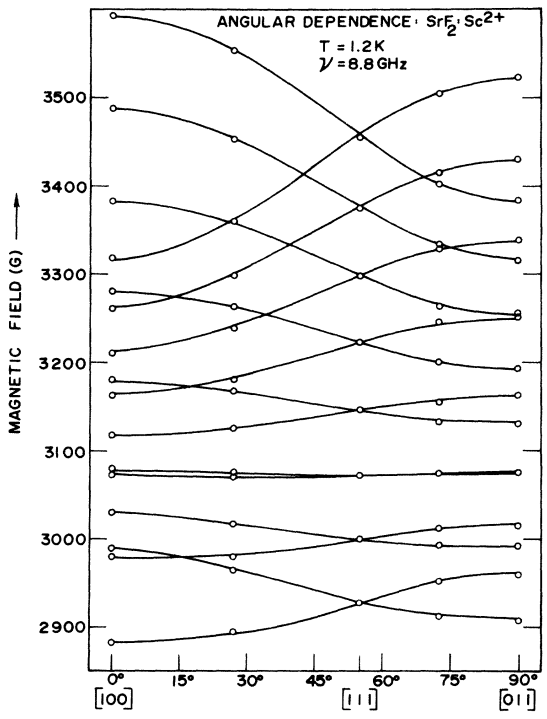


FIG. 6. Angular dependence of the extremes for the anisotropic pattern observed for $SrF_2:Sc^{2+}$. The open circles are experimental measurements and the solid curves were computed using the parameters in Table I for $SrF_2:Sc^{2+}$ and Eq. (2). All values of the strain angular parameter $\phi$ were assumed to occur with equal probability.

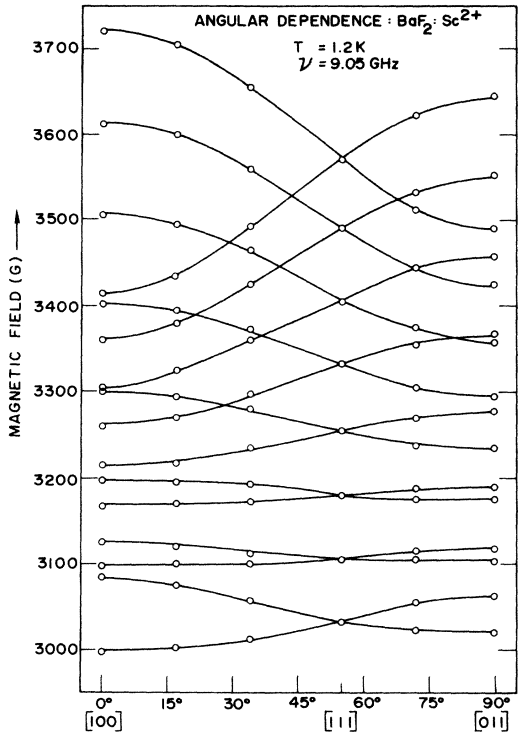


FIG. 7. Angular dependence of the extremes for the anisotropic pattern observed for $BaF_2:Sc^{2+}$. The open circles are experimental measurements and the solid curves were computed using the parameters in Table I for $BaF_2:Sc^{2+}$ and Eq. (2). All values of the strain angular parameter $\phi$ were assumed to occur with equal probability.

is relatively large for the $Sc^{2+}$ systems.

## IV. IMPLICATIONS OF THE WEAK-TO-MODERATE VIBRONIC COUPLING MODEL

The EPR spectra reported here are characteristic of an isolated $^2E$ state in cubic symmetry. A $^2E$ ground state is predicted by conventional crystal-field theory for ions with $d^1$ configurations in eightfold coordination. Ham has shown[3,13] that the symmetry classification of the ground vibronic state for an electronic $^2E$ state with weak-to-moderate vibronic coupling is also $^2E$. The only experimental evidence for the existence of a weak-to-moderate vibronic interaction is the observation that certain experimental parameters are reduced from the values predicted in the absence of vibronic coupling, i.e., by conventional crystal-field theory. It is the purpose of this section to compare the observed reductions in the parameters measured for $Sc^{2+}$ in $CaF_2$, $SrF_2$, and $BaF_2$ and to indicate that the implied strengths of the vibronic coupling are physically reasonable. Many of the calculations presented in this section are extremely rough and are presented merely to show consistency between the experimental data and Ham's weak-to-moderate vibronic coupling model.[3,13] The data previously reported[17,19] for $SrCl_2:La^{2+}$, $SrCl_2:Y^{2+}$, and $SrCl_2:Sc^{2+}$ are included for comparison purposes.

Conventional crystal-field theory predicts the following first-order expressions for the parame-

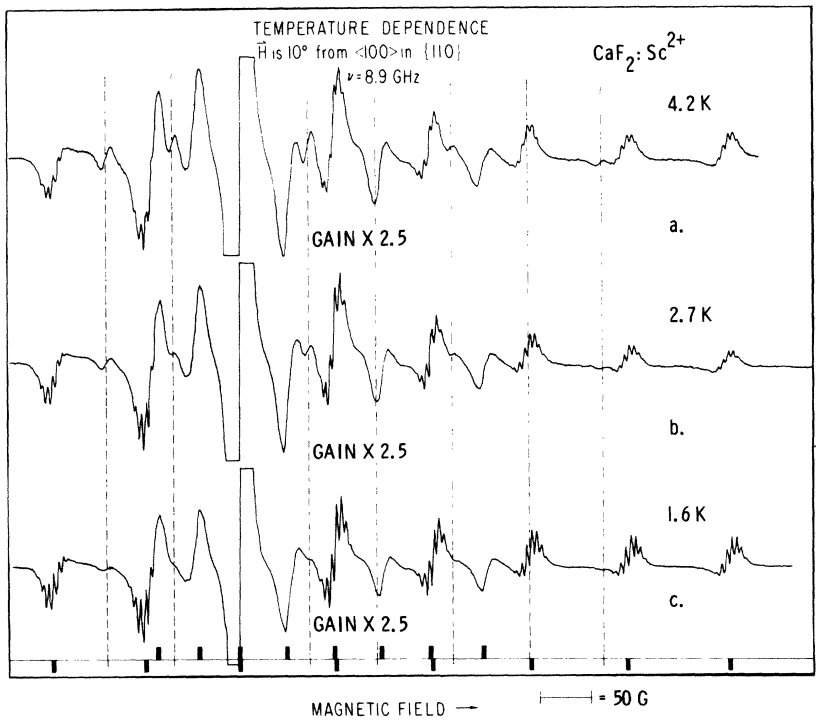


FIG. 8. Temperature dependence of the EPR spectrum observed from a reduced $CaF_2:Sc^{2+}$ sample for (a) $T=4.2$ K, (b) $T=2.7$ K, and (c) $T=1.6$ K. The dashed vertical lines locate the eight lines due to the averaging of a portion of the anisotropic pattern produced by rapid vibronic relaxation. The extremes of the components of the anisotropic pattern are designated by vertical bars. The first derivative of absorption is shown versus magnetic field for the magnetic field oriented 10° from a ⟨100⟩ axis in a {110} plane.

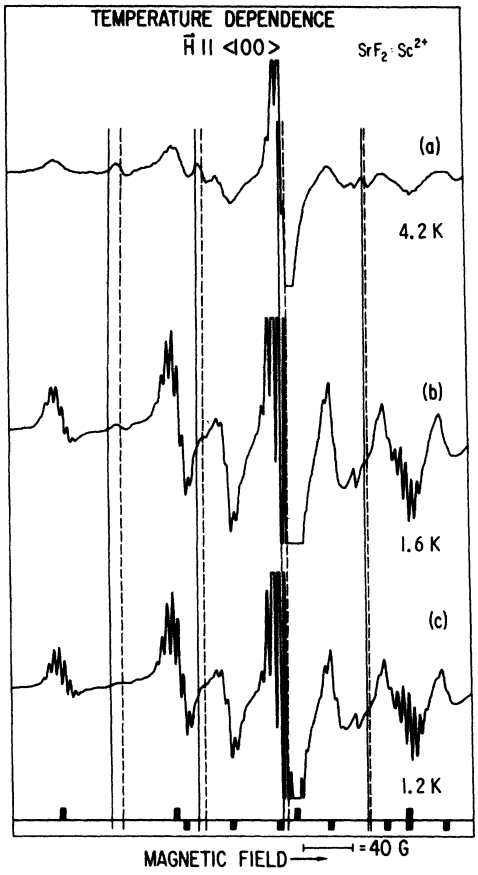


FIG. 9. Temperature dependence of a portion of the EPR spectrum observed from a reduced $SrF_2:Sc^{2+}$ sample for: (a) 4.2 K, (b) 1.6 K, and (c) 1.2 K. The first derivative of absorption is shown versus magnetic field for the magnetic field aligned parallel to a $\langle 100 \rangle$ axis. The dashed vertical lines locate the components of the "averaged" pattern while the solid vertical lines denote the positions of the hyperfine lines observed for $\vec{H} \parallel \langle 111 \rangle$. The extremes of the components of the anisotropic pattern are designated by vertical bars.

ters, $g_1$, $g_2$, $A_1$, $A_2$ and $Q$ for a $d^1$-configuration ion in eightfold cubic coordination:

$$g_1 = 2.0023 - 4\lambda/\Delta \,, \tag{9}$$

$$g_2 = -4\lambda/\Delta = g_1 - 2.0023 \,, \tag{10}$$

$$A_1 = (-2\mu_B\mu \langle r^{-3} \rangle / I)(\kappa + 4\lambda/\Delta) \,, \tag{11}$$

$$A_2 = (-2\mu_B\mu \langle r^{-3} \rangle / I)\,(\tfrac{4}{7} + \tfrac{34}{7}\lambda/\Delta) \,, \tag{12}$$

$$Q = \frac{2e^2Q_N}{7I(2I-1)} \langle r^{-3} \rangle \,. \tag{13}$$

The parameters $\lambda$, $\Delta$, $\mu_B$, $\mu$, $I$, $\langle r^{-3} \rangle$, $\kappa$, $e$, and $Q_N$ are respectively the spin-orbit coupling constant, the cubic-crystal-field splitting $10Dq$, the Bohr magneton, the nuclear magnetic dipole moment, the nuclear spin, the one-electron expectation value of $r^{-3}$, the Fermi contact parameter, the electron charge, and the nuclear-electric quadrupole moment.

The reduction factor $q$, included explicitly in the parameters, $qg_2$, $qA_2$, and $qQ$ in Table I, may be estimated from the experimental parameters, $g_1$ and $qg_2$. The reduction factors for the various systems are listed in Table II. They are related to the strength of the vibronic interaction and hence the Jahn-Teller stabilization energy $E_{JT}$. In particular a decrease in $q$ from unity toward $\frac{1}{2}$ corresponds to an increase in the ratio $E_{JT}/\hbar\omega$. Estimates of the ratio, $E_{JT}/\hbar\omega$, were made and are listed in Table II. Using the value 300 $cm^{-1}$ for $\hbar\omega$ (the approximate average optical-phonon energy for the alkaline-earth halides), the estimates of the vibronic coupling strength parameter $V_{JT}$ listed in Table II were obtained.

The relatively small variations in $q$ (and hence in $E_{JT}$ and $V_{JT}$) implied by the EPR data for the $Sc^{2+}$ ions in the fluoride hosts and the lack of a definite correlation between these reduction factors and the fluoride lattice constants, indicate that the vibronic interaction itself is essentially independent of the nearest-neighbor spacing for these systems. However, the appreciable difference between $q$ for $Sc^{2+}$ in $SrCl_2$ and the $q$'s for $Sc^{2+}$ in the fluoride hosts implies that though the vibronic interaction does not depend strongly on the lattice constant of the host, it does depend on the electron affinity of the anions.

Dividing the parameters $qg_2$, $qA_2$, and $qQ$ listed in Table I by the appropriate reduction factor $q$, one obtains estimates for the parameters $g_2$, $A_2$, and $Q$. These estimates, together with the parameters $g_1$ and $A_1$ given in Table I, can be used in Eqs. (9)–(13) to calculate the values for $\kappa$, $\langle r^{-3} \rangle$, $\mu$, and $Q_N$ given in Table II. The systematic variations in these parameters are physically reasonable, and the predicted values for the nuclear moments agree remarkably well with currently accepted values which are shown in parentheses in Table II.

The measured EPR parameters reported here and elsewhere[17–19] for $SrCl_2:Sc^{2+}$, $CaF_2:Sc^{2+}$, $SrF_2:Sc^{2+}$, $BaF_2:Sc^{2+}$, $SrCl_2:Y^{2+}$, and $SrCl_2:La^{2+}$ are all consistent with the following model, which is illustrated schematically in Fig. 11: (1) The $^2D$ free-ion term of the $nd^1$ configuration in eightfold coordination is split by the cubic-crystal-field interaction into a ground $^2E$ electronic state and a $^2T_2$ excited electronic state separated by energies on the order of $10^4$ $cm^{-1}$. (2) The ground vibronic state resulting from a weak-to-moderate linear vibronic interaction ($E_{JT}/\hbar\omega \simeq 0.05$ to 1.0) is a $^2E$ state with the first excited state on the order of $10^2$ $cm^{-1}$ above the ground state. (3) Owing to large random internal strains (on the order of

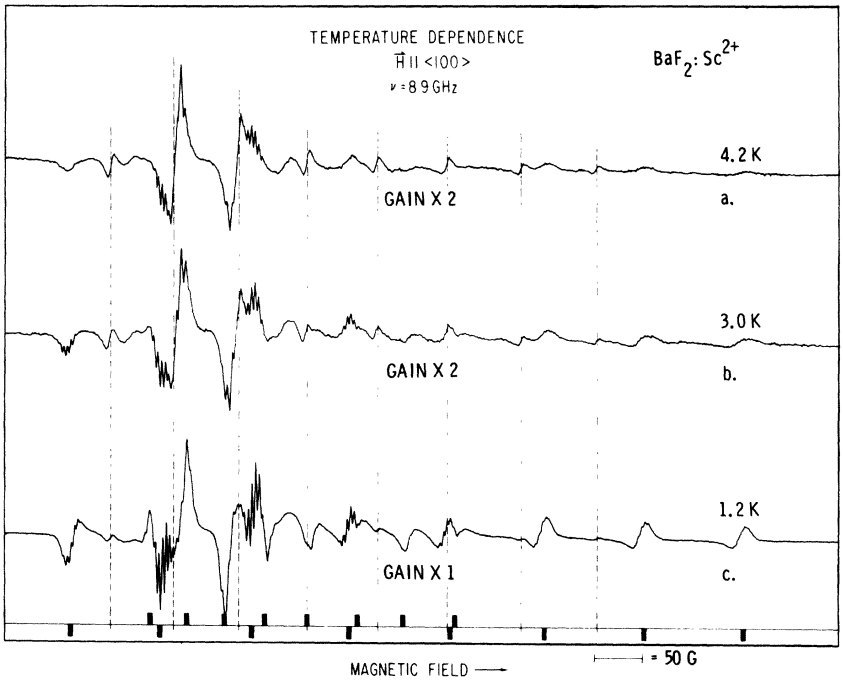


FIG. 10. Temperature dependence of the EPR spectrum observed from a reduced $BaF_2:Sc^{2+}$ sample for: (a) $T=4.2$ K, (b) $T=3.0$ K, and (c) $T=1.2$ K. The first derivative of absorption is shown versus magnetic field for the magnetic field aligned parallel to a $\langle 100\rangle$ axis. The dashed vertical lines locate the components of the "averaged" pattern while the extremes of the components of the anisotropic pattern are designated by vertical bars. Note the difference in gain used for trace (c).

$10^{-4}$ to $10^{-5}$), the $^2E$ vibronic state is split into two Kramers doublets which are separated by about 1 $cm^{-1}$. This strain splitting varies from ion site to ion site because of a distribution in strain magnitude. (4) The Kramers degeneracy is removed by the applied magnetic field, and the magnitude of the Zeeman splitting depends on the ratio of the strain components, $e_\theta$ and $e_\epsilon$ and on the orientation of the magnetic field. (5) The microwave absorption consists of complex envelopes of transitions (indicated in Fig. 11 by solid arrows). The shapes of these envelopes depend on the distribution of the strain angular parameter, $\phi$, and all values of this quantity occur with equal probability. (6) Owing to rapid vibronic relaxation (indicated in Fig. 11 by wavy arrows), a portion of these complex envelopes is averaged.

## V. SUMMARY AND CONCLUSIONS

EPR spectra have been observed for $BaF_2:Sc^{2+}$, $SrF_2:Sc^{2+}$, and $CaF_2:Sc^{2+}$. The spectra observed from $CaF_2:Sc^{2+}$ and $SrF_2:Sc^{2+}$ are similar to those previously reported by Höchli and Estle,[12] and Höchli.[13] Each EPR spectrum consisted of three different patterns: (a) an intense eight-component anisotropic pattern, (b) a weak eight-line "nearly"

TABLE II. Summary of parameters calculated from the experimental effective Hamiltonian parameters in Table I using the weak-to-moderate vibronic coupling model. Numbers shown in parentheses are the currently accepted values which are to be compared with the calculated values.

| Host : Defect | $\lambda$[a] ($cm^{-1}$) | $\Delta$[b] ($cm^{-1}$) | $q$[c] | $E_{JT}/\hbar\omega$[d] | $V_{JT}$[e] ($cm^{-1}$) | $\kappa$ | $\langle r^{-3}\rangle$ ($10^{22}$ $G^2$/erg) | $\mu$ (nuclear magnetons) | $Q_N$ (b) |
|---|---|---|---|---|---|---|---|---|---|
| $CaF_2:Sc^{2+}$ | 79 | 10 000 | 0.69 | 0.4 | 4000 | 1.1 | 0.5 | +5(+4.75)* | −0.30(−0.22) |
| $SrF_2:Sc^{2+}$ | 79 | 8 000 | 0.63 | 0.5 | 5000 | 1.1 | 0.5 | +5(+4.75) | −0.30(−0.22) |
| $BaF_2:Sc^{2+}$ | 79 | 7 000 | 0.66 | 0.5 | 5000 | 1.1 | 0.5 | +5(+4.75) | −0.30(−0.22) |
| $SrCl_2:Sc^{2+}$ | 79 | 6 000 | 0.86 | 0.1 | 2000 | 1.1 | 0.5 | +5(+4.75) | −0.30(−0.22) |
| $SrCl_2:Y^{2+}$ | 300 | 15 000 | 0.65 | 0.5 | 5000 | 2.1 | 0.6 | −0.2(−0.14) | ... |
| $SrCl_2:La^{2+}$ | 640 | 20 000 | 0.57 | 1.0 | 7000 | 2.4 | 0.7 | +2.5(+2.76) | +0.30(+0.20) |

[a]Computed from the $^2D_{5/2}$-$^2D_{3/2}$ free-ion spin-orbit splitting listed in NBS Circ. No. 467.
[b]Computed from $g_1$ in Table I and the free-ion $\lambda$ using Eq. (9).
[c]Computed from $g_1$ and $g_2$ in Table I using Eqs. (9) and (10).
[d]Extrapolated from Fig. 5 of Ref. 3.
[e]Computed from $E_{JT}/\hbar\omega$ assuming $\hbar\omega=300$ $cm^{-1}$ using Eq. 2.3.3 of Ref. 3.

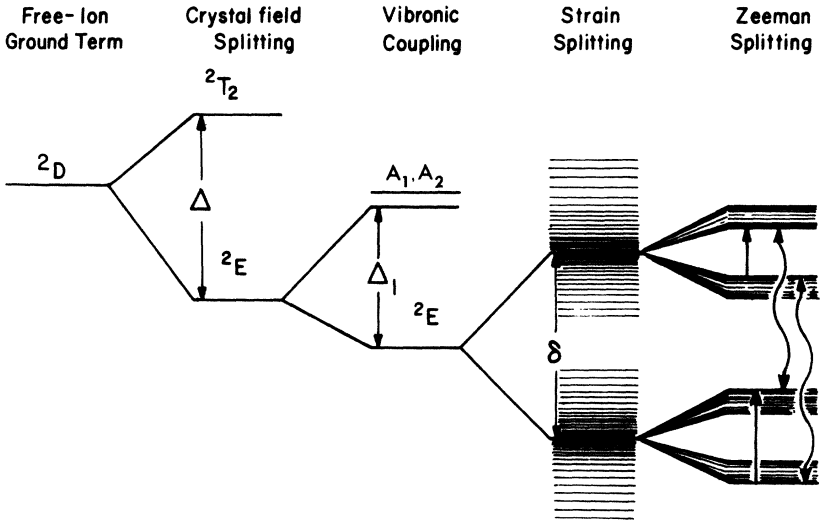


FIG. 11. Schematic energy-level diagram implied by the interpretation of the EPR parameters. The $^2D$ free-ion term is split by the cubic crystal field into $^2E$ and $^2T_2$ states with the $^2E$ state lowest. A weak-to-moderate vibronic interaction results in a series of vibronic states and the ground vibronic state is also a $^2E$ state. The first excited vibronic state is sufficiently far from the ground state to enable one to treat the ground state as an isolated $^2E$ state. This state is split by random internal strains into two Kramers doublets. The Kramers degeneracy is removed by an applied magnetic field and EPR transitions (represented by straight arrows) are induced by the microwave magnetic field. The wavy arrows represent vibronic relaxation processes which can produce an averaging of a portion of the anisotropic EPR pattern. This type of relaxation should not be confused with spin-lattice relaxation.

isotropic pattern, and (c) a very weak seven-component pattern observed only for $\vec{H} \parallel \langle 111 \rangle$.

The line shapes, anisotropy, and temperature dependence of the strong eight-component anisotropic pattern were described within experimental error by second-order solutions of an effective Hamiltonian for an isolated $^2E$ state. Random internal strains were dominant in determining the composition of the vibronic states. Ligand hyperfine structure was observed with eight $^{19}F$ nuclei of spin $\frac{1}{2}$. Distortions of the line shapes of the hyperfine components produced by second-order terms in the solution of the effective Hamiltonian may influence the resolution of the ligand hyperfine structure. The analysis and the experimental parameters describing the spectra were found to be consistent with the suggestion by Ham[3,8] that the vibronic coupling was not sufficiently strong to necessitate the use of the tunneling model.

Weak, nearly isotropic hyperfine lines were observed to coexist with the intense anisotropic pattern at low temperatures. Variations in the intensities of these weak lines as a function of temperature, the observation of a small predicted anisotropy in their field positions, and the total lack of resolved ligand hyperfine structure, imply that they result from averaging of a portion of the anisotropic pattern by vibronic relaxation.

The seven very weak lines observed for $\vec{H} \parallel \langle 111 \rangle$ have been discussed previously[18] and were shown to be $\Delta M_S = \pm 1$, $\Delta M_I = \pm 1$ transitions. Variations in the positions and intensities of these lines imply the existence of a nuclear electric quadrupole interaction for cubic-symmetry defects exhibiting a dynamic Jahn-Teller effect.

In conclusion, the principal features of the EPR spectrum due to $Sc^{2+}$ in $CaF_2$, $SrF_2$, and $BaF_2$ may be described within experimental error by an isolated vibronic doublet. Observed reductions of certain parameters from the values predicted by conventional crystal-field theory imply the existence of a weak-to-moderate vibronic interaction, i.e., a dynamic Jahn-Teller effect.

## ACKNOWLEDGMENTS

We gratefully acknowledge the valuable technical assistance of E. G. Clardy and the useful comments of Dr. R. W. Reynolds, Dr. B. Dischler, G. G. Setser, and R. Mier-Maza on the manuscript. In addition, we thank the office of Naval Research for the contribution of helium used in the initial stages of this work. Also, we would like to thank Dr. R. J. Shalek and the M. D. Anderson Hospital of the University of Texas for permitting our use of their $^{137}Cs$ source for sample irradiation.

*Work supported in part by the National Science Foundation and the National Aeronautics and Space Administration.

†A portion of the work was performed while at Rice University, Houston, Texas 77001.

‡Present address: Physics Dept., University of Illinois, Urbana, Ill. 61801.

[1]H. A. Jahn and E. Teller, Proc. R. Soc. Lond. A 161, 220 (1937).

[2]A review of both the experimental results and theory related to the Jahn-Teller effect is contained in the article by M. D. Sturge, in *Solid State Physics*, edited by F. Seitz, D. Turnbull, and H. Ehrenreich (Academic, New York, 1967), Vol. 20.

[3]The theory of the Jahn-Teller effect and the experimental results obtained by electron spin resonance have been reviewed by F. S. Ham, in *Electron Paramagnetic Resonance*, edited by S. Geschwind (Plenum, New York, 1972).

[4]R. E. Coffman, Phys. Lett. 19, 475 (1965).

[5]R. E. Coffman, Phys. Lett. 21, 381 (1966).

[6]R. E. Coffman, J. Chem. Phys. 48, 609 (1968).

[7]R. E. Coffman, D. L. Lyle, and D. R. Mattison, J. Chem. Phys. 72, 1392 (1968).

[8]U. T. Höchli and T. L. Estle, Phys. Rev. Lett. 18, 128 (1967).

[9]U. T. Höchli, Phys. Rev. 162, 262 (1967).

[10]I. B. Bersuker, Zh. Eksp. Teor. Fiz. 43, 1315 (1962) [Sov. Phys.-JETP 16, 933 (1963)].

[11]I. B. Bersuker, Zh. Eksp. Teor. Fiz. 44, 1239 (1963) [Sov. Phys.-JETP 17, 836 (1963)].

[12]M. C. M. O'Brien, Proc. R. Soc. Lond. A 281, 323 (1964).

[13]F. S. Ham, Phys. Rev. 166, 307 (1968).

[14]L. L. Chase, Phys. Rev. Lett. 23, 275 (1969).

[15]L. L. Chase, Phys. Rev. B 2, 2308 (1970).

[16]J. R. Herrington, T. L. Estle, L. A. Boatner, and B. Dischler, Phys. Rev. Lett. 24, 984 (1970).

[17]J. R. Herrington, T. L. Estle, and L. A. Boatner, Phys. Rev. B 3, 2933 (1971).

[18]J. R. Herrington, T. L. Estle, and L. A. Boatner, Phys. Rev. B 5, 2500 (1972).

[19]J. R. Herrington, T. L. Estle, and L. A. Boatner, Phys. Rev. B 7, 3003 (1973).

[20]T. J. Aton, J. R. Herrington, T. L. Estle, and L. A. Boatner, Bull. Am. Phys. Soc. 16, 386 (1971).